Supporting Information

Scrolling reduced graphene oxides to induce room temperature magnetism via spatial coupling of defects

Ting Shi[1], Yuan Yao[1*], Yang Hong[1], Yang Li[1], Songtao Lu[1], Wei Qin[2] and Xiaohong Wu[1*]

[1]MIIT Key Laboratory of Critical Materials Technology for New Energy Conversion and Storage, School of Chemistry and Chemical Engineering, Harbin Institute of Technology, Harbin, Heilongjiang 150001, P. R. China.

[2]School of Materials Science and Engineering, Harbin Institute of Technology, Harbin, Heilongjiang 150001, P. R. China.

*E-mail: yyuan@hit.edu.cn (Y.Y.); wuxiaohong@hit.edu.cn (X.W.)

The Supporting Information file includes:

Contents **Page**

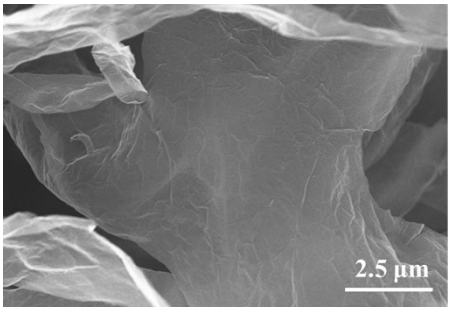

Fig. S1 SEM image of GO.

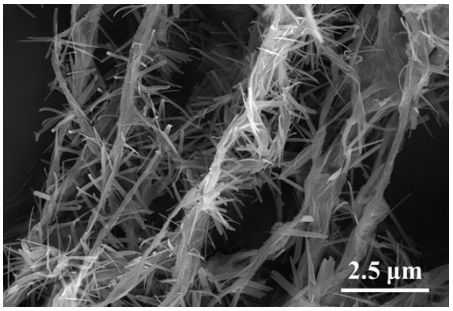

Fig. S2 SEM image of original GO nanoscrolls.

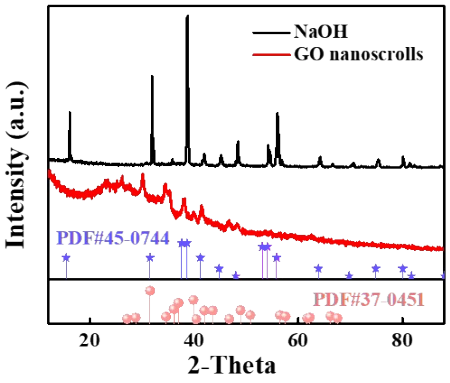

Fig. S3 XRD patterns of NaOH and original GO nanoscrolls.

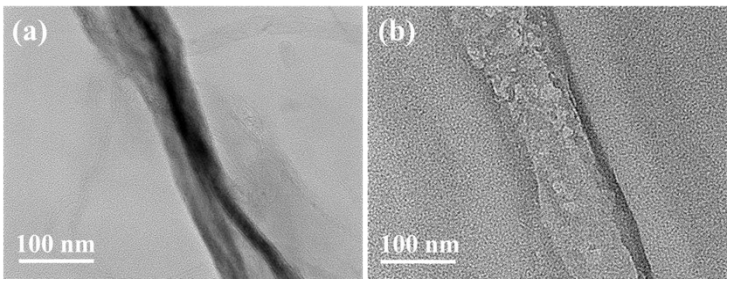

Fig. S4 TEM images of (a) DR-rGO nanoscrolls-350 and (b) DR-rGO nanoscrolls-750.

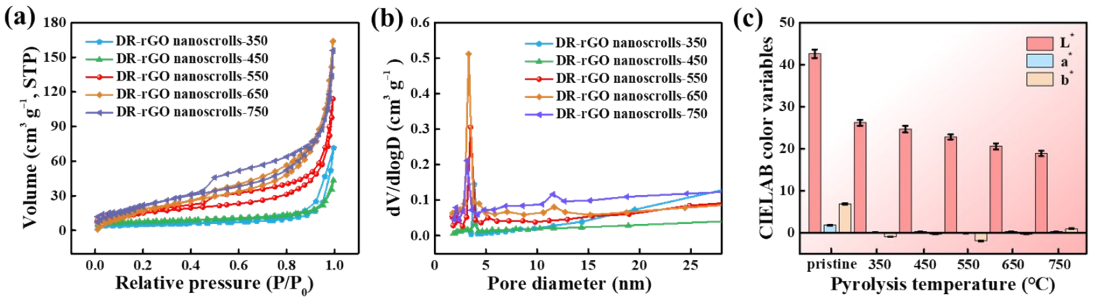

86

87 **Fig. S5** (a) N_2 adsorption-desorption profiles, (b) pore size distributions, (c) CIELAB color variable values of DR-

88 rGO nanoscrolls-X (X=350, 450, 550, 650 and 750), respectively. The error bars represent the standard deviation of

89 the measured data and reflect the measurement accuracy.

90 The CIELAB color variables (*i.e.*, L*, a*, and b*) exhibited a certain change as the

91 increase of pyrolysis temperature. Among them, brightness factor (L*) for DR-rGO

92 nanoscrolls-750 changed from 42.6 (original GO nanoscrolls) to 18.8, implying an

93 increase in surface blackness and reduction degree during elevated pyrolysis

94 temperature.

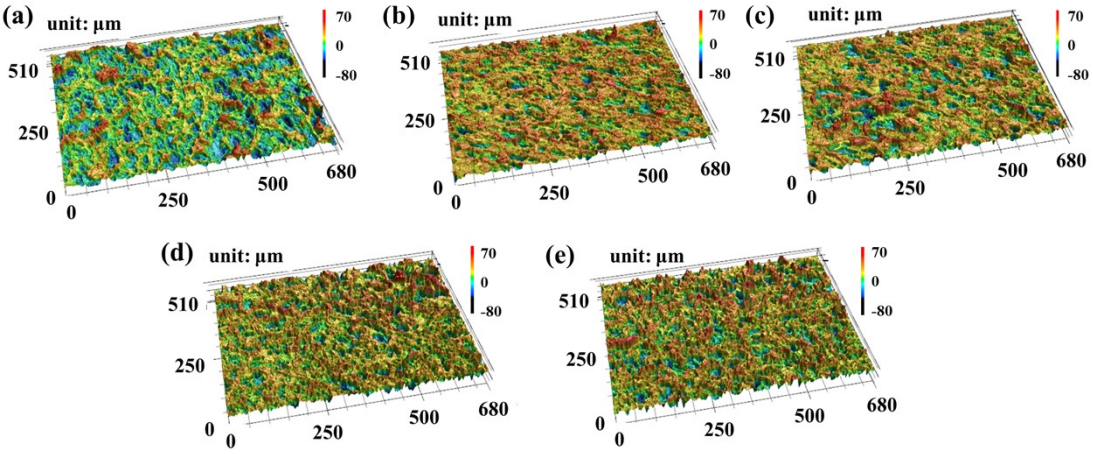

95

96 **Fig. S6** (a–e) 3D laser confocal scanning images of DR-rGO nanoscrolls-X (X=350, 450, 550, 650 and 750),

97 respectively.

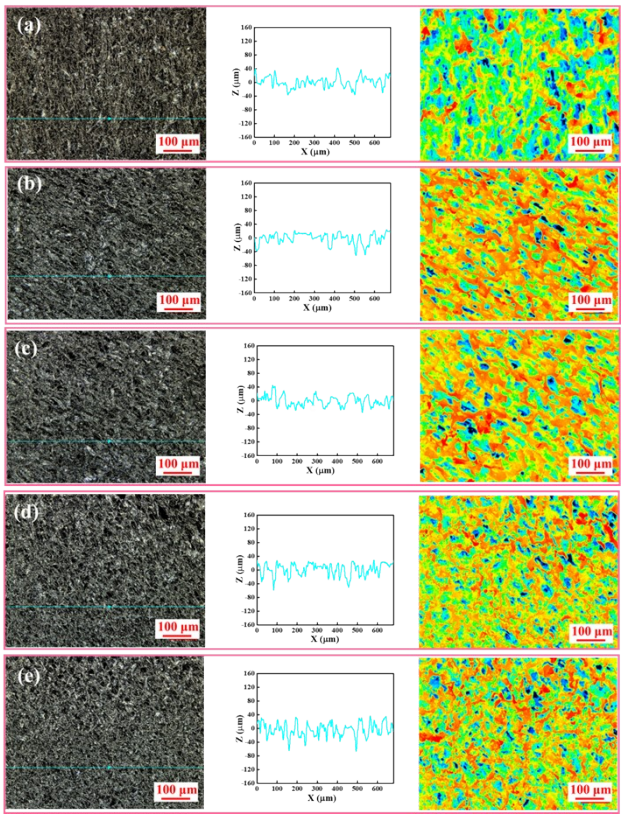

Fig. S7 (a–e) 3D laser confocal scanning images, the respective roughness line profiles of DR-rGO nanoscrolls-X (X=350, 450, 550, 650 and 750), respectively. We used the probe line that vertically intersects the interface along the direction of blue line.

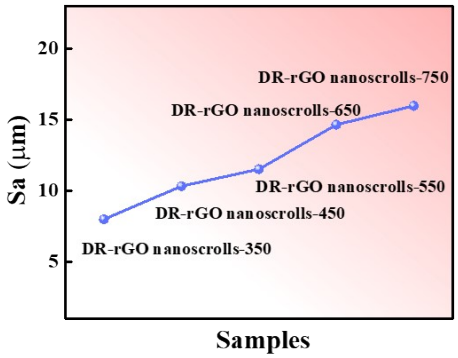

Fig. S8 The arithmetic mean height (Sa) of DR-rGO nanoscrolls-X (X=350, 450, 550, 650 and 750).

The interfacial structures of these aerogels were further analyzed by roughness measurement.[1,2] The roughness tracing line profiles of all samples showed the characteristics of up and down oscillations within ±40 μm (Fig. S7), indicating that their macrostructures were void-rich.

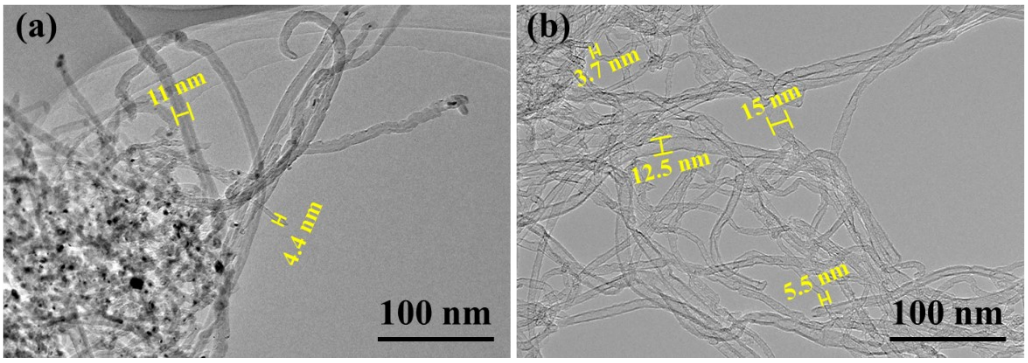

108

109 **Fig. S9** (a) TEM image of CNTs before acidification and washing process, containing a small amount of metal

110 nanoparticles. (b) TEM image of CNTs used to be involved in nanoscrolls, showing no magnetic impurities after

111 acidification and the washing process.

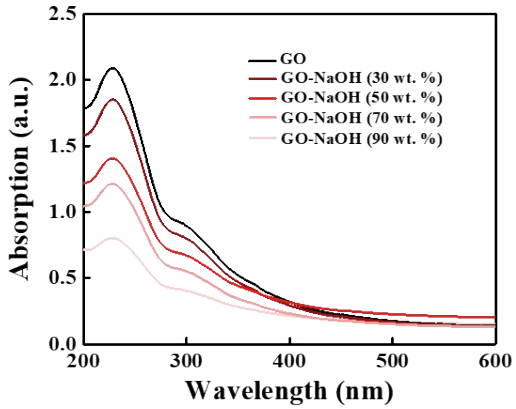

112

113 **Fig. S10** UV-Vis spectra of GO suspension with different content of NaOH.

Note S1: Derjaguin-Landau-Verwey-Overbeek (DLVO) theory

$$\Phi_{\text{Total}} = \Phi_{\text{vdw}} + \Phi_{\text{EDL}} \quad \text{(S1)}$$

$$\Phi_{\text{vdw}} = -\frac{A}{12\pi h^2} \quad \text{(S2)}$$

$$\Phi_{\text{EDL}} = \varepsilon_0 \varepsilon_{\text{w}} k \psi^2 \left[\frac{1}{\sinh(kh)} + 1 - \coth(kh) \right] \quad \text{(S3)}$$

$$k^{-1} = \sqrt{\frac{\varepsilon_0 \varepsilon_{\text{w}} k_{\text{B}} T}{2 N_{\text{A}} e^2 I}} \quad \text{(S4)}$$

The aqueous solution of GO is a colloidal solution essentially.[3] Therefore, the phenomenon of aggregation and separation can be analyzed by DLVO theory.[4] The total potential energy (Φ_{Total}) is equal to the attractive van der Waals interaction (Φ_{vdW}) plus the repulsive electrostatic double-layer interaction (Φ_{EDL}). The van der Waals interaction was calculated by the equation (S2). Electro-static double-layer interaction can be calculated by equation (S3). Debye reciprocal length k (nm^{-1}) can be calculated by equation (S4).

A is the Hamaker constant (6.26×10^{-21} J); h is the separation distance between two particles; ε_0 is the vacuum permittivity (8.854×10^{-12} C V^{-1} m^{-1}), ε_{w} is the relative dielectric permittivity of water (78.5); The zeta potential value was used to replace the surface potential approximately. k_{B} is Boltzmann's constant (1.38064852×10^{-23} J K^{-1}); T is the temperature (300 K), N_{A} is the Avogadro number (6.022140857×10^{23} mol^{-1}), e is the electron charge ($1.6021766208\times10^{-19}$ C), and I is ionic strength in the unit of mol L^{-1}.

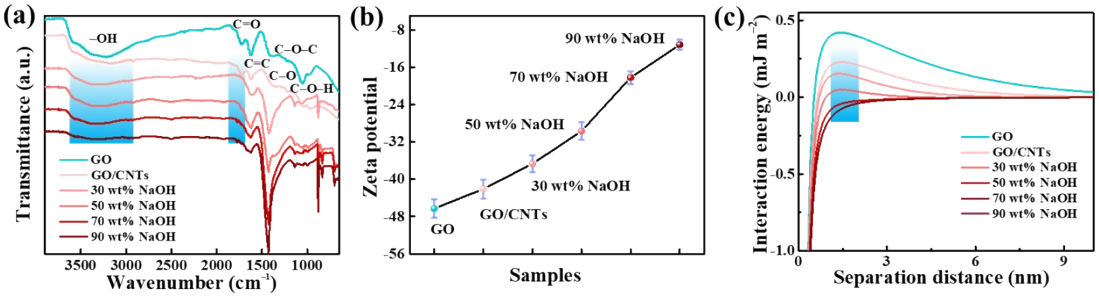

Fig. S11 (a) FTIR spectra of GO-based aerogel with different NaOH contents, (b) Zeta potential and (c) DLVO interaction profiles of GO sheets with different NaOH contents. The date in Fig. S11b shows mean ± SD of test solution at steady state. The error bars represent the standard deviation of the measured data and reflect the measurement accuracy.

FTIR spectra revealed the changes of functional groups in aerogel after freeze-drying. As shown in Fig. S11a, after the addition of NaOH, the absorption peaks located at 3370 cm^{-1}, 1736 cm^{-1}, 1210 cm^{-1}, and 848 cm^{-1} got weakened, indicating that oxygen-containing groups in the scroll were reduced, proving that NaOH has a weak reduction effect on GO.[5,6] The higher the concentration of hydroxide is, the more obvious the reduction effect is.

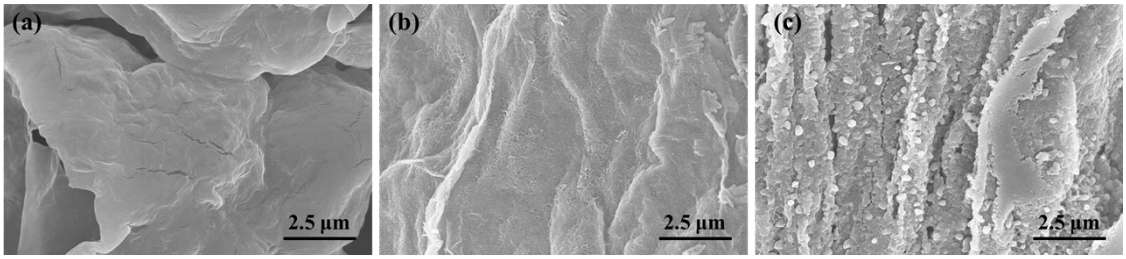

Fig. S12 SEM images of GO aerogels under different NaOH contents: (a) 30 wt%, (b) 70 wt%, and (c) 90 wt%.

148 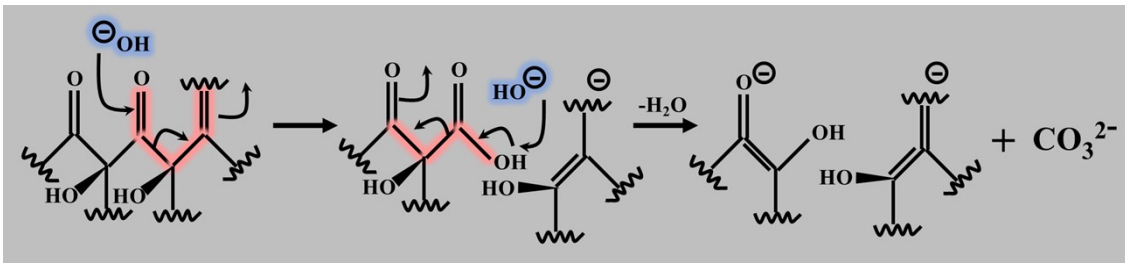

149 **Fig. S13** Schematic showing the decarboxylation of GO under mild alkaline conditions.

150 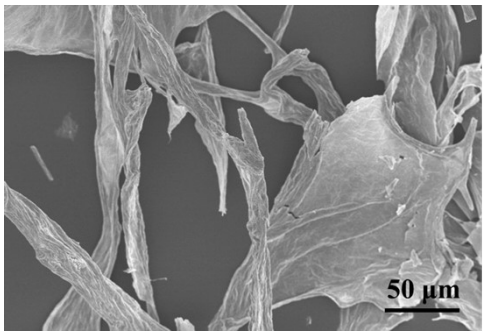

151 **Fig. S14** SEM image of GO nanoscrolls aerogel through refrigerator freezing.

152

Note S2: Electron paramagnetic resonance (EPR) spectra and Brillouin function

EPR spectra of free radicals are usually characterized by a single wide resonance.[7] In this case, it is possible to obtain the g value, line width, and spin concentration. The g value of the EPR spectrum can be used to determine whether the radical is a carbon center, carbon-centered with adjacent oxygen atoms, or oxygen-centered.[8] The fundamental equation:

$$E=h\nu=g\beta_e B_0 \quad \text{(S5)}$$

Where defines the value of g, where h is Planck constant, ν is the constant microwave frequency applied in the experiment, β_e is the Bohr magneton, and B_0 is the resonant magnetic field. The g value of free electrons is 2.00232. The change of g value is related to the magnetic interaction, involving the orbital angular momentum of unpaired electrons and their chemical environment.

The M–H curve is fitted using the Brillouin function.[9]

$$M = NgJ\mu_B\left[\frac{2J+1}{2J}\coth\left(\frac{2J+1}{2J}x\right)-\frac{1}{2J}\coth\left(\frac{x}{2J}\right)\right] \quad \text{(S6)}$$

where $x=gJ\mu_B H/k_B T$, g is the Landau factor which is assumed to be 2, J is the angular momentum number, N is the number of spins, and k_B is the Boltzmann constant.

Fitting the M–H curve by Brillouin function, the spin density can be obtained. The spin density values of DR-rGO nanoscrolls-X can be deduced (Fig. S17d), which are 2.32×10^{19}, 2.39×10^{19}, 3.77×10^{19}, 1.86×10^{19}, and 1.73×10^{19} spins g^{-1}, respectively. Therefore, the spin density fitted by Brillouin function is in good agreement with the experimental results of EPR, which further indicates that the magnetic moment comes from the unpaired spin.

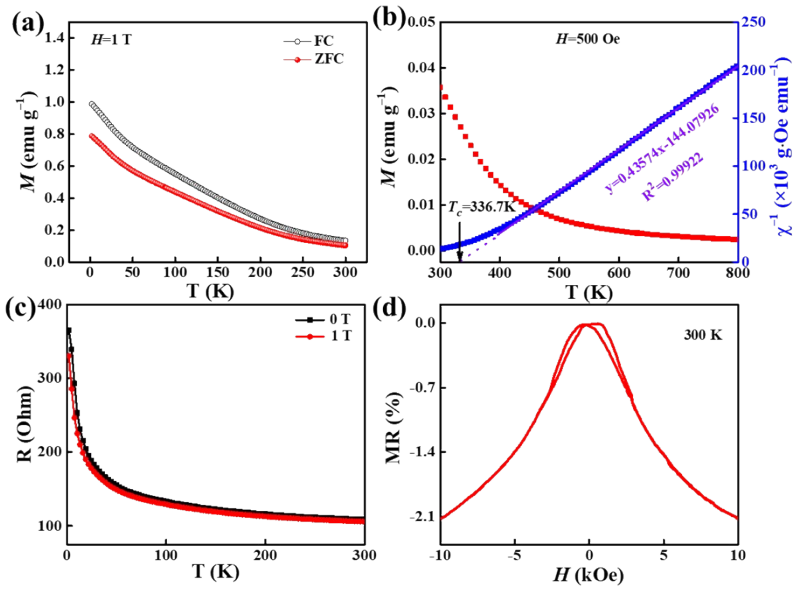

175

176 **Fig. S15** (a) Field cooled (FC) and zero field cooled (ZFC) curves of DR-rGO nanoscrolls-550 at 2~300 K under

177 applied field *H*=1 T. (b) Temperature dependence of magnetization (*M*–T) and the inverse susceptibility in the

178 300~800 K with a measured field for 500 Oe of DR-rGO nanoscrolls-550. It obeys Curie-Weiss law above 336.7 K

179 and has more than 99 % reliability. (c) Temperature-dependent resistance under 0 T and 1 T magnetic fields at the

180 temperature range from 2 K to 300 K for DR-rGO nanoscrolls-550. (d) The field dependent MR for DR-rGO

181 nanoscrolls-550 at 300 K.

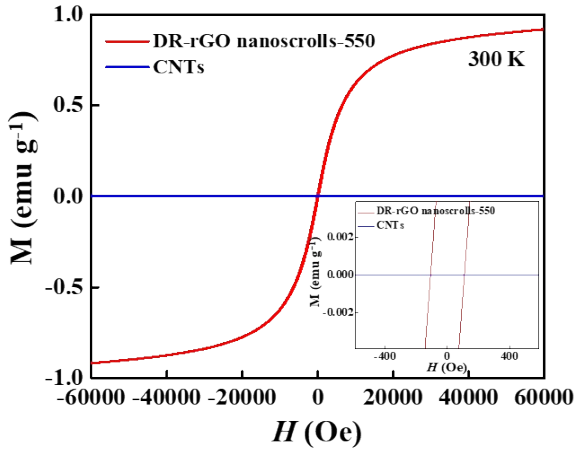

182

183 **Fig. S16** *M–H* curves measured at 300 K. The red line represents the DR-rGO nanoscrolls-550. Blue line represents

184 the CNTs used to be involved in nanoscrolls. The inset shows the *M–H* curves in a narrow scale for better perception.

185 The CNTs were polished by an acid treatment and washing process to remove the

186 residual metal nanoparticles. 2 g CNTs were added into HNO_3/H_2SO_4 (1/3, v/v) mixture

187 with sonication treatment for 30 min. The mixture was then refluxed at 343 K for 4 h.

188 After cooling, the mixing solution was repeatedly washed with DI water until the pH

189 reached ~7.

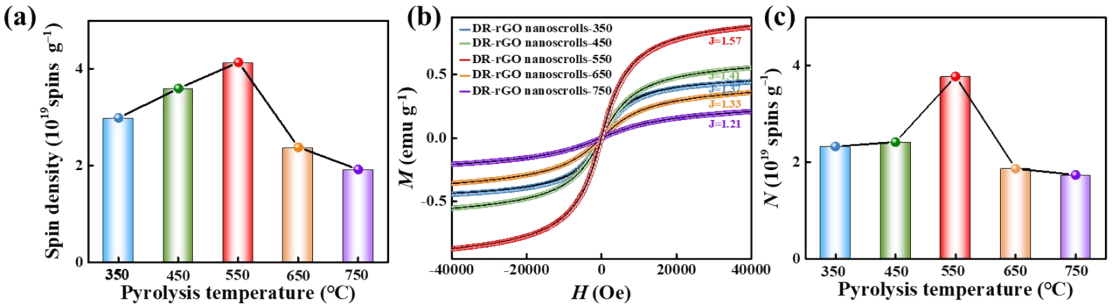

190

191 **Fig. S17** (a) Spin density of DR-rGO nanoscrolls-X (X=350, 450, 550, 650 and 750) from EPR spectrometer. (b) *M*–

192 *H* curve measured at 300 K. Symbols are the measurements and black solid curve is fit to the Brillouin function with

193 *g*=2. (c) Spin density extracted from the Brillouin fits.

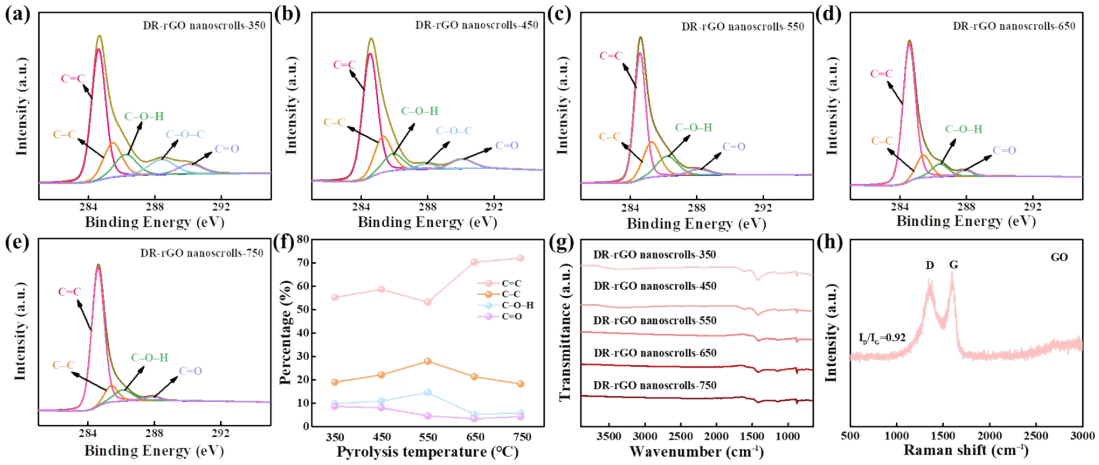

194

195 **Fig. S18** (a–e) High-resolution C1s XPS spectra of DR-rGO nanoscrolls-X (X=350, 450, 550, 650 and 750),

196 respectively. (f) Comparison of C=C, C–C, C–O–H, and C=O content in DR-rGO nanoscrolls-X (X=350, 450, 550,

197 650 and 750). C–O of DR-rGO nanoscrolls-350/450 contain two components (C–O–H and C–O–C). C–O of DR-

198 rGO nanoscrolls-550/650/750 contain a single component (C–O–H). (g) FTIR spectra of DR-rGO nanoscrolls-X

199 (X=350, 450, 550, 650 and 750). (h) Raman spectra of original GO.

200 As shown in Fig.2i and Fig. S18a,b, DR-rGO nanoscrolls-350/450 can be

201 deconvoluted into five peaks (C=C sp^2, C–C sp^3, C–O–H, C–O–C, and C=O). As for

202 DR-rGO nanoscrolls-550/650/750 (Fig. S18c~e), this can be deconvoluted into 4 peaks

203 (C=C sp^2, C–C sp^3, C–O–H, and C=O).[10] The detected C-sp^3 peaks mean the presence

of intrinsic defects in these samples, and their intensity usually determines the proportion of intrinsic defects.[11,12] The DR-rGO nanoscrolls-550 have the highest percentage of C-sp^3 which not only supports the formation of numerous intrinsic defects, but also confirms that both carbonization temperature have a significant effect on C-sp^2/sp^3 content.

Fig. 2j and Fig. S18h present the spectrum of DR-rGO nanoscrolls and GO with D peak, G peak, and 2D peak which are consistent with literature reports.[2,14] The G peak, represents the in-plane vibrational mode of the sp^2 carbon atom. D peak is affected by defects. I_D/I_G is usually used as an indicator of the lattice defect density of carbon materials. The more lattice defects are, the higher the intensity ratio of I_D/I_G is. It started increasing for the samples DR-rGO nanoscrolls-350. The biggest I_D/I_G ratio (1.02) was observed for DR-rGO nanoscrolls-550. As for DR-rGO nanoscrolls-650/750, the I_D/I_G values were decreased to 0.99 and 0.98, respectively. This is because defects had started mending themselves by a self-repair mechanism, where carbon adatoms acquired enough energy to fill up the vacancy, and the reconstruction of C–C bonds took place.[15] As all know, defects are closely related to lone pair, and they usually show magnetism.[16] The largest I_D/I_G value indicates that DR-rGO nanoscrolls-550 have a higher proportion of intrinsic defects, which is in good agreement with the results of XPS and EPR.

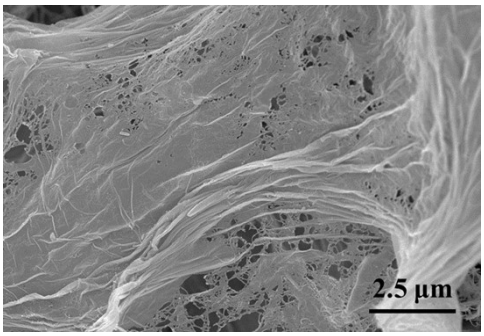

Fig. S19 SEM image of DR-rGO nanosheets-550.

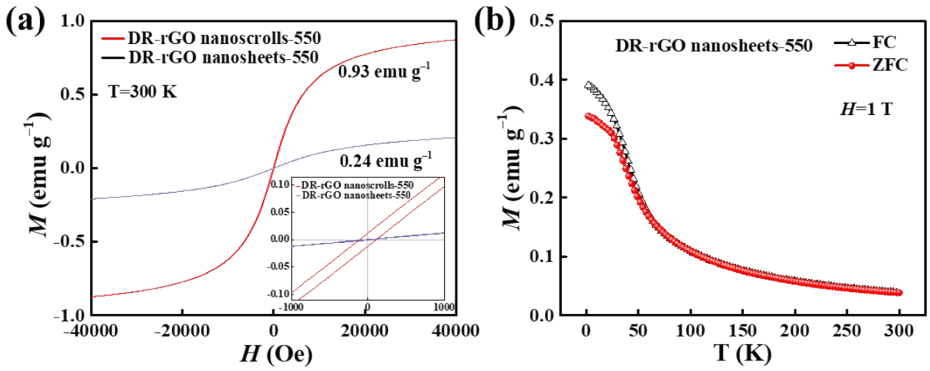

Fig. S20 (a) *M*–*H* curves of DR-rGO nanoscrolls-550 and DR-rGO nanosheets-550 under static external magnetic fields ranging from −6 T to +6 T at 300 K. The inset is the magnification of the *M*–*H* curves at low magnetic fields. (b) ZFC/FC curves for DR-rGO nanosheets-550 from 2 to 300 K under the applied field *H*=1 T.

Note S3: DFT calculation details

All the calculations were carried out by the Vienna Ab initio Simulation Package (VASP5.4.4).[17] The electron exchange-correlation was processed within the framework of generalized gradient approximation (GGA) in the Perdew–Burke–Ernzerhof (PBE) parametrization.[18] The electron-ion interaction was described using the projected augmented wave (PAW) method. The plane-wave cutoff energy was set to be 600 eV. To avoid the interactions between periodic images, a vacuum space of 15 Å along c directions was set for the slab. The Brillouin zone integrations were performed with 2×1×1 (structure optimization) and 6×3×3 (density of states) G point- centred k-point Monkhorst-Pack meshes. The convergence criterion wave cutoff was set to 10^{-5} eV. Blue and yellow isosurfaces represent positive (0.007 e $Å^{-3}$) and negative (0.001 e $Å^{-3}$) spin densities, respectively. In addition, the structure models were visualized in the VESTA software.

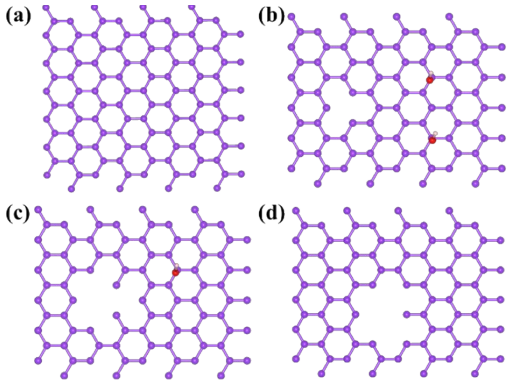

Fig. S21 Calculation model. (a) Pristine graphene. (b) Defective graphene with two hydroxy (removed one carbon atom). (c) Defective graphene with one hydroxy (removed four carbon atoms). (d) Defective graphene with the number of removed five carbon atoms. The purple, red, and white colours represent carbon, oxygen, and hydrogen atoms, respectively.

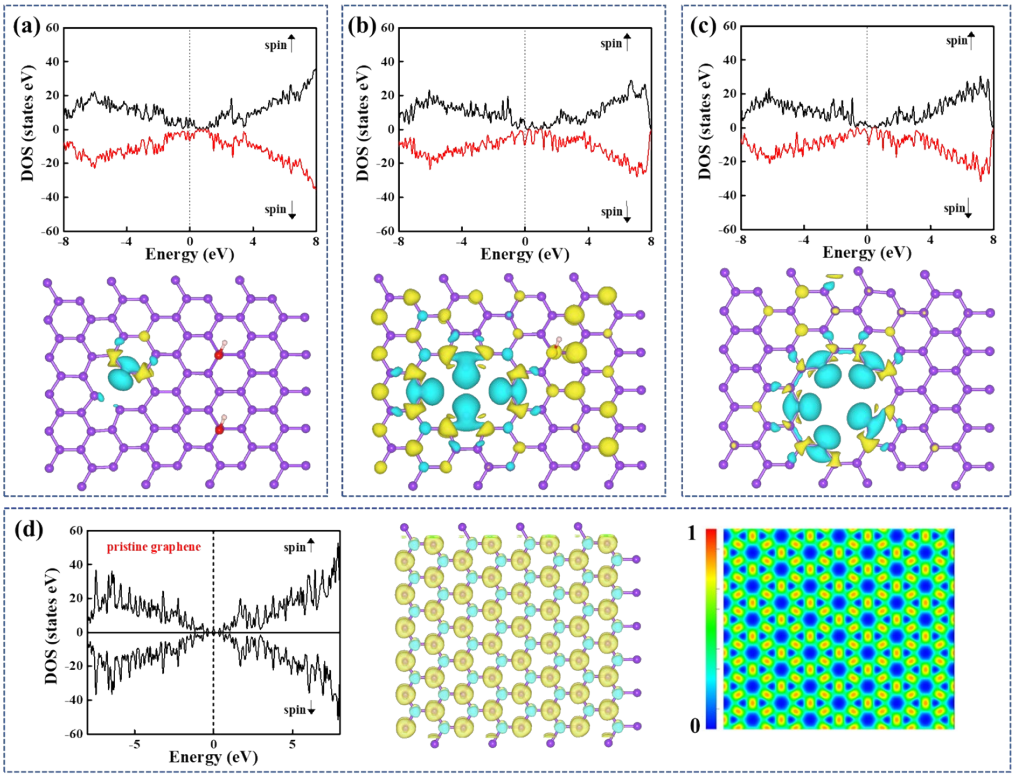

Fig. S22 DOS plot and spatial distribution of spin density for (a) defective graphene with two hydroxy (removed one carbon atom), (b) defective graphene with one hydroxy (removed four carbon atoms), and (c) defective graphene with the number of removed five carbon atoms. (d) DOS plot, spatial distribution of spin density, and electron localization function for pristine graphene.

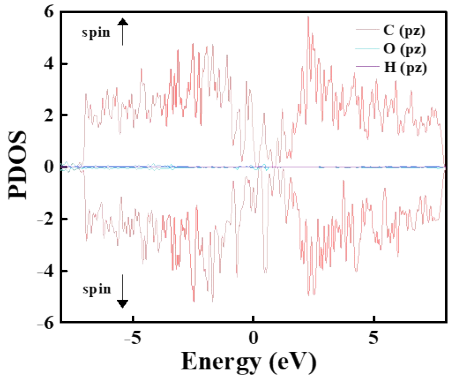

254

255 **Fig. S23** Partial densities of states for defective graphene with one hydroxy (removed four carbon atoms).

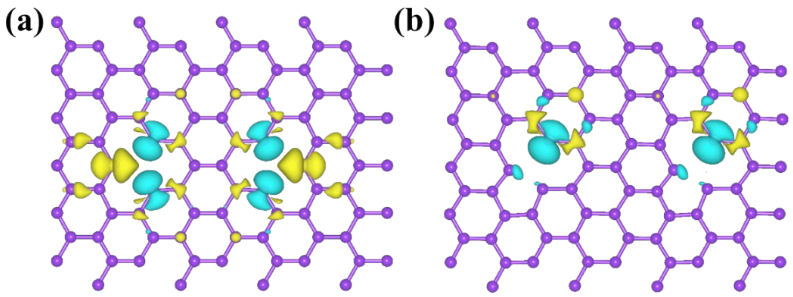

256

257 **Fig. S24** The spatial distribution of spin density for different configurations. (a) Ferromagnetism (The positions of

258 the two defects are separated by two carbon atoms). (b) Ferromagnetism (The positions of the two defects are

259 separated by three carbon atoms), indicating that the coupling depends on the relative positions.

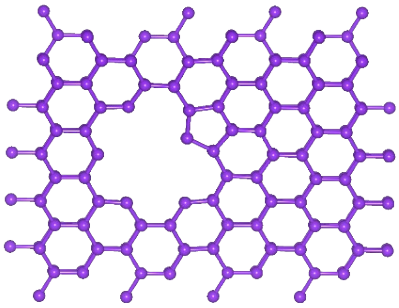

260

261 **Fig. S25** Calculation model of bilayer defective graphene (removed four carbon atoms).

262

Note S4: Electromagnetic wave (EMW) absorption

For the investigation of EMW attenuation properties, electromagnetic parameters were measured by the coaxial method. The melted paraffin quickly infiltrates and penetrated into the 3D structure by capillary action, and then presses into a ring with an outer diameter of 7 mm and an inner diameter of 3 mm. The EMW absorption performance was evaluated based on the transmission line theory,[19,20] as shown in the following equation:

$$\mathrm{RL(dB)} = 20\lg\left|\frac{Z_{\mathrm{in}} - Z_0}{Z_{\mathrm{in}} + Z_0}\right| \tag{S7}$$

$$Z_{\mathrm{in}} = Z_0\sqrt{\frac{\mu_{\mathrm{r}}}{\varepsilon_{\mathrm{r}}}}\tanh\left[\mathrm{j}\frac{2\pi fd}{c}\sqrt{\mu_r\varepsilon_r}\right] \tag{S8}$$

$$Z_0 = \sqrt{\frac{\mu_0}{\varepsilon_0}} \tag{S9}$$

$$\alpha = \left(\frac{\sqrt{2}\pi f}{c}\right)\sqrt{(\mu''\varepsilon'' - \mu'\varepsilon') + \sqrt{(\mu''\varepsilon'' - \mu'\varepsilon')^2 + (\varepsilon'\mu'' + \varepsilon''\mu')^2}} \tag{S10}$$

where Z_{in}, Z_0, f, c, ε_r, and μ_r is input impedance, the impedance of the air, microwave frequency, the velocity of light in free space, and the relative permittivity and permeability, respectively. The EMW absorption mechanism could be clarified by analyzing the complex permittivity (ε_r=ε'–jε'') and complex permeability (μ_r=μ'–jμ''). The real parts ε' and μ' represent the storage capability of electric and magnetic energies, while the imaginary parts ε'' and μ'' stand for the dissipation capability of electric and magnetic energies. Generally, the microwave absorption performances are evaluated using the reflection loss ($\mathrm{RL_{min}}$) and effective absorption bandwidth (EAB, the bandwidth of RL ≤ −10 dB). Ideal impedance matching requires a $|\mathrm{Z_{in}/Z_0}|$ value of 1.0 that implies the complete entrance of incident electromagnetic wave into absorber.

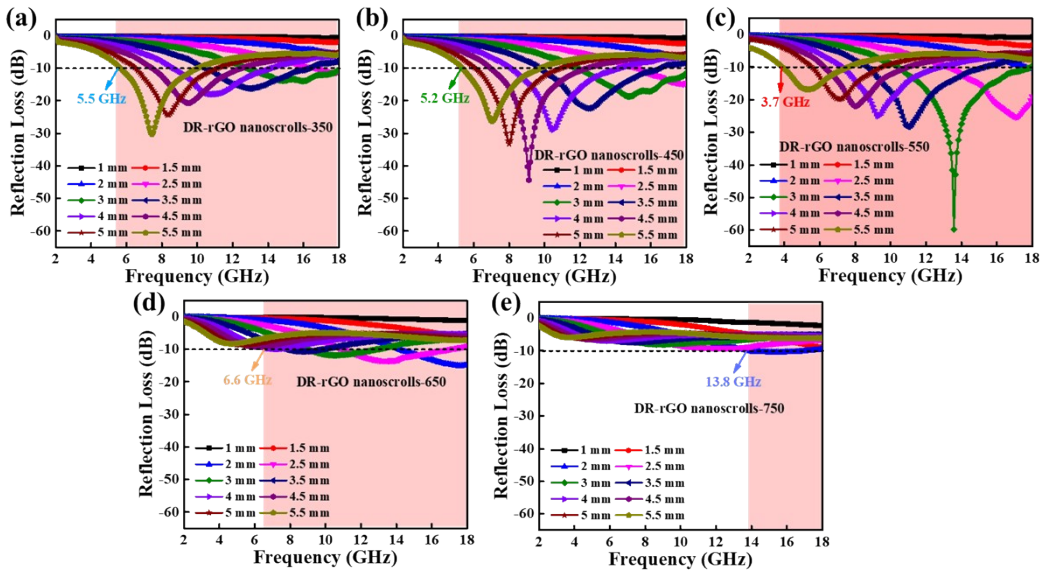

284

285 **Fig. S26** (a–e) 2D RL for DR-rGO nanoscrolls-X (X=350, 450, 550, 650 and 750), respectively.

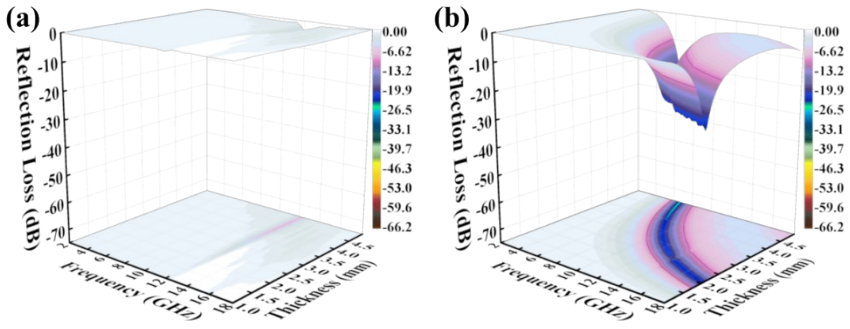

286

287 **Fig. S27** 3D RL for (a) defect-free GO nanoscrolls and (b) DR-rGO nanosheets-550.

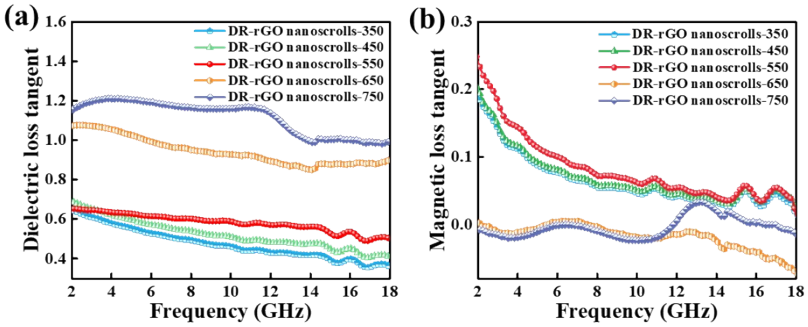

288

289 **Fig. S28** (a) Dielectric loss tangent and (b) Magnetic loss tangent for DR-rGO nanoscrolls-X (X=350, 450, 550,

290 650 and 750).

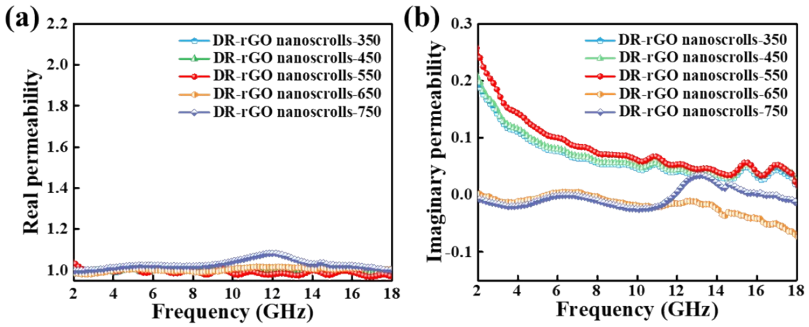

291

292 **Fig. S29** Electromagnetic parameters of DR-rGO nanoscrolls-X (X=350, 450, 550, 650 and 750). (a) Real part, (b)

293 imaginary part of the complex permeability.

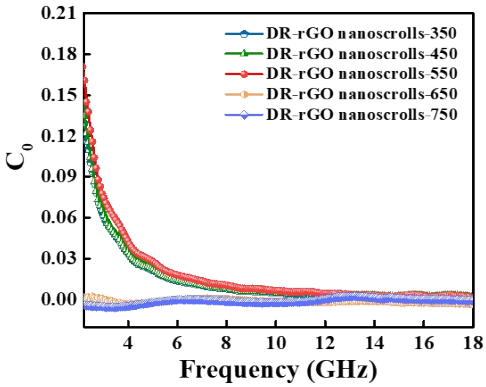

294

295 **Fig. S30** Eddy current loss (C_0) for DR-rGO nanoscrolls-X (X=350, 450, 550, 650 and 750).

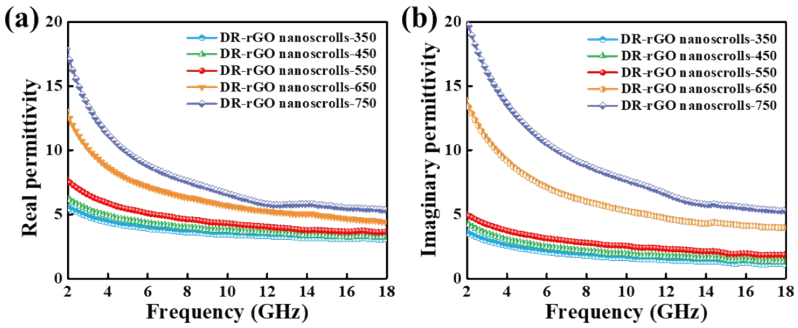

296

297 **Fig. S31** Electromagnetic parameters of DR-rGO nanoscrolls-X (X=350, 450, 550, 650 and 750): (a) Real part. (b)

298 Imaginary part of the complex permittivity.

299

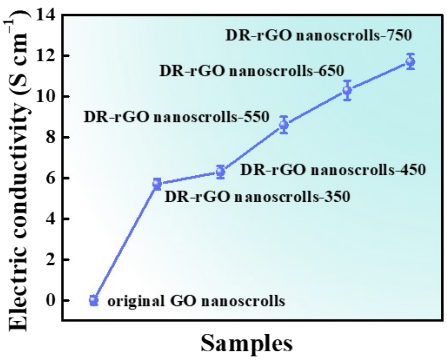

300

301 **Fig. S32** Electric conductivity for original GO nanoscrolls and DR-rGO nanoscrolls-X (X=350, 450, 550, 650 and

302 750).

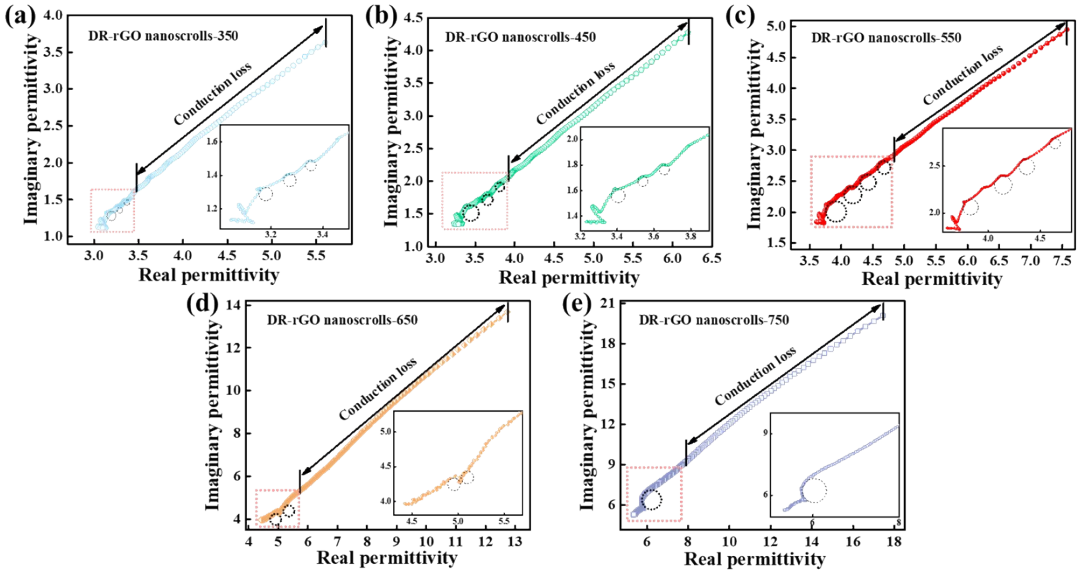

303

304 **Fig. S33** (a–e) Cole-Cole curves for DR-rGO nanoscrolls-X (X=350, 450, 550, 650 and 750), respectively. The inset

305 is the enlarged graph of the Cole-Cole curves at the lower left corner in the high-frequency region.

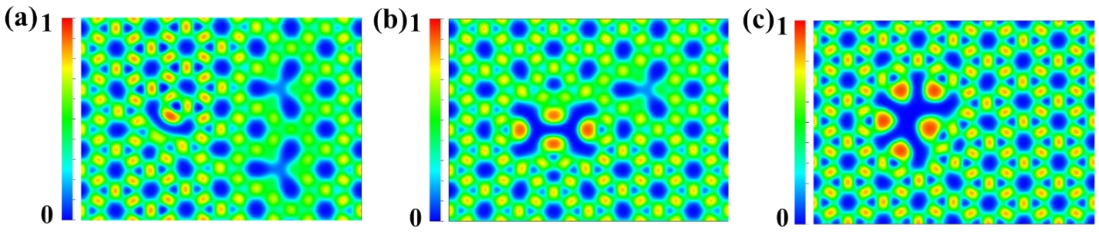

306

307 **Fig. S34** Electronic local function diagrams of (a) Defective graphene with two hydroxy (removed one carbon atom).

308 (b) Defective graphene with one hydroxy (removed four carbon atoms). (c) Defective graphene with the number of

309 removed five carbon atoms.

310 **Table S1.** Experiments with different contents of NaOH.

NaOH/wt%	(GO+CNTs)/wt%
30	70
50	50
70	30
90	10

311

312 **Table S2.** Magnetic properties of graphene-based materials.

Materials	M_s (emu g^{-1})	Temperature	Type of magnetism
Co embedded N-doped graphene[21]	0.11	300 K	FM
N-doped graphene[22]	1.09	69 K	FM
N-doped graphene quartz fabrics[23]	0.14	300 K	FM
RGO[24]	0.26	9.77	FM
Graphene-600[25]	0.02	300 K	FM
Nanomesh graphene[26]	0.04	300 K	FM
Hydrogenated graphene[27]	0.006	-	FM
Graphene nanoribbons[28]	0.25	5 K	FM
N-doped graphene[29]	0.014	300 K	FM
GO nanoribbons[13]	0.39	300 K	FM
DR-rGO nanoscrolls-550	**0.93**	**300 K**	**FM**

313

314 **Table S3.** Concentrations of the selected metals in the DR-rGO nanoscrolls samples, as determined by ICP-MS.

Sample	Fe (ppm)	Co (ppm)	Ni (ppm)	Mn (ppm)
DR-rGO nanoscrolls-350	9.76	2.52	10.01	8.87
DR-rGO nanoscrolls-450	7.63	5.43	8.21	5.33
DR-rGO nanoscrolls-550	7.17	8.75	13.10	9.13
DR-rGO nanoscrolls-650	11.32	9.77	10.67	13.78
DR-rGO nanoscrolls-750	10.23	6.16	10.24	9.18

315

316 **Table S4.** Performance comparison of the different EMW absorption materials.

Materials	RL_{min}	EAB	Thickness	Filler loading
Nitrogen-doped graphene[30]	–11.3	2.1	3	30
RGO@anthraquinone[31]	–54.2	7.0	3	10
N-doped rGO@CNTs[32]	–49.4	7.1	1.4	2
N/B co-doped rGO [33]	–52.0	6	2.8	5
PANi/ND[34]	–46.0	12	4.3	-
Peel-based carbon aerogel[35]	–29.5	5.8	1.7	20
WC/carbon composites[36]	–55.6	4.9	1.5	45
MXene/magnetic CNTs [37]	–51.98	7.76	1.9	14.2
NbS_2[38]	–43.85	6.48	2.07	40
ACET filled NiCu-MOFs[39]	–40.54	5.87	2.5	40
$Fe/Fe_3O_4@C$[40]	–55.4	4.2	3	50
Ferrite crystallites/Fe[41]	–53.5	8	2	50
$Ti_3C_2T_x$ MXene@Ni[42]	–59.6	4.48	1.5	-
Co/chitosan-GO[43]	–45.02	4.02	1.5	30
N-Doped Co/C[44]	–42.3	5.1	1.9	-
Metal single atoms[45]	–46.2	4.7	-	10
MoS_2/MXene aerogel[46]	–61.65	5.9	4.53	-
$Co_{1.29}Ni_{1.71}O_4$[47]	–50.7	4.84	1.6	50
MnO@N-doped CNTs[48]	–62.8	5.4	2.4	60
graphene aerogel fibers[10]	–27.9	9.69	2.5	
Fe/Fe_3C[49]	–46.0	3.76	2.9	30
Ceramic metamaterials[50]	–36.33	6.8	1.9	35
SiCO coated BN[51]	–55.6	8.7	4	1
$NiO/NiCo_2O_4$[52]	–48.1	5.84	1.86	50
Glassmicrospheres@Co_2SiO_4[53]	–46.7	5.92	2.9	20
NiAl-LDH/graphene[54]	–41.5	4.4	1.4	7
DR-rGO nanoscrolls-550	**–62.1**	**7.8**	**3.0**	**3**

317

318 **Table S5.** Performance comparison of graphene-based dielectric materials.

Materials	RL_{min}	EAB	Thickness	Filler loading
Graphene Nanocages[55]	–51.1	4.4	1.45	25
Hollow graphene aerogel[56]	–52.7	9.3	2.3	5
N-Doping porous graphene aerogel[57]	–56.4	6.8	2.35	6
Porous graphene sheet[58]	–56.4	6.4	3.0	4
Defective graphene[59]	–43.11	6.4	5.0	0.52
WS_2/CNT-rGO[60]	–56.63	3.84	1.15	30
RGO@ANF[61]	–56.5	7.0	2.8	1.7
N-BCMT/RGO[62]	–55.45	8.36	3.2	2
SiC/multilayer graphene[63]	–53.62	0.82	2.0	20
Graphene nanoribbon/PVDF foams[64]	–54.1	2.8	5.17	15
Porous rGO/BN/SiC[65]	–37.8	5.9	2.9	8
MW-rGO[66]	–54.11	5.68	2	5
Graphene aerogels[67]	–52.6	7.65	4.8	3
RGO/GDY[68]	–58	4.3	1.9	27.5
DR-rGO nanoscrolls-550	**–62.1**	**7.8**	**3.0**	**3**

319

References

1 C. Luo, H. Zheng, L. Wang, H. Fang, J. Hu, C. Fan, Y. Cao and J. Wang, *Angew. Chem. Int. Ed.*, 2010, 49, 9145–9148.

2 H. Liu, T. Xu, C. Cai, K. Liu, W. Liu, M. Zhang, H. Du, C. Si and K. Zhang, *Adv. Funct. Mater*, 2022, 32, 2113082.

3 B. Sun, Y. Zhang, W. Chen, K. Wang and L. Zhu, *Environ. Sci. Technol*., 2018, 52, 7212–7219.

4 H. Tang, Y. Zhao, X. Yang, D. Liu, P. Shao, Z. Zhu, S. Shan, F. Cui and B. Xing, *Environ. Sci. Technol.*, 2017, 51, 9674–9682.

5 L. B. A. Ayrat M. Dimiev, and James M. Tour., *ACS Nano*, 2012, 7, 576–588.

6 S. Eigler, S. Grimm, F. Hof and A. Hirsch, *J. Mater. Chem. A*, 2013, 1, 11559–11562.

7 M. Roessler and E. Salvadori, *Chem. Soc. Rev.*, 2018, 47, 2534–2553.

8 U. Green, K. Keinan-Adamsky, S. Attia, Z. Aizenshtat, G. Goobes, S. Ruthstein and H. Cohen, *Phys. Chem. Chem. Phys.*, 2014, 16, 9364–9370.

9 R. Nair, M. Sepioni, I. Tsai, O. Lehtinen, J. Keinonen, A. Krasheninnikov, T. Thomson, A. Geim and I. Grigorieva, *Nat. Phys.*, 2012, 8, 199–202.

10 Y. Hou, Z. Sheng, C. Fu, J. Kong and X. Zhang, *Nat. Commun.*, 2022, **13**, 1227.

11 C. Li, Z. Zhang, Y. Chen, X. Xu, M. Zhang, J. Kang, R. Liang, G. Chen, H. Lu, Z. Yu, W. J. Li, N. Wang, Q. Huang, D. Zhang, S. L. Chou and Y. Jiang, *Adv. Sci.*, 2022, **9**, e2104780.

12 H. Sun, L. Mei, J. Liang, Z. Zhao, C. Lee, H. Fei, M. Ding, J. Lau, M. Li, C. Wang, X. Xu, G. Hao, B. Papandrea, I. Shakir, B. Dunn, Y. Huang and X. Duan, *Science*, 2017, **356**, 599–604.

13 L. Fu, Y. Wang, K. Zhang, W. Zhang, J. Chen, Y. Deng, Y. Du and N. Tang, *ACS Nano*, 2019, **13**, 6341–6347.

14 Y. Xu, C. Y. Chen, Z. Zhao, Z. Lin, C. Lee, X. Xu, C. Wang, Y. Huang, M. I. Shakir and X. Duan, *Nano Lett.*, 2015, **15**, 4605–4610.

15 B. Song, G. F. Schneider, Q. Xu, G. Pandraud, C. Dekker and H. Zandbergen, *Nano Lett.*, 2011, **11**, 2247–2250.

16 J. Tucek, P. Blonski, J. Ugolotti, A. K. Swain, T. Enoki and R. Zboril, *Chem. Soc. Rev.*, 2018, **47**, 3899–3990.

17 J. F. G. Kresse, *Phys. Rev. B*, 1996, **54**, 11169–11186.

18 K. B. John P. Perdew, Matthias Ernzerhof., *Phys. Rev. Lett*, 1996, **77**, 3865–3868.

19 Y. Xia, W. Gao and C. Gao, *Adv. Funct. Mater.*, 2022, **32**, 2204591.

20 X. Wang, W. Cao, M. Cao and J. Yuan, *Adv. Mater.*, 2020, **32**, 2002112.

21 W. Hu, C. Wang, H. Tan, H. Duan, G. Li, N. Li, Q. Ji, Y. Lu, Y. Wang, Z. Sun, F. Hu and W. Yan, *Nat. Commun.*, 2021, **12**, 1854.

22 P. Blonski, J. Tucek, Z. Sofer, V. Mazanek, M. Petr, M. Pumera, M. Otyepka and R. Zboril, *J. Am. Chem. Soc*, 2017, **139**, 3171–3180.

23 Y. Xie, S. Liu, K. Huang, B. Chen, P. Shi, Z. Chen, B. Liu, K. Liu, Z. Wu, K. Chen, Y. Qi and Z. Liu, *Adv. Mater.*, 2022, **34**, e2202982.

24 S. Kim, H. Kim, K. Lee, K. Roh, J. Han, K. Kim, S. Lee and M. Jung, *Carbon*, 2019, **142**, 373–378.

25 Y. Wang, Y. Huang, Y. Song, X. Zhang, Y. Ma, J. Liang and Y. Chen, *Carbon*, 2009, **9**, 220–224.

26 G. Ning, C. Xu, L. Hao, O. Kazakova, Z. Fan, H. Wang, K. Wang, J. Gao, W. Qian and F. Wei, *Carbon*, 2013, **51**, 390–396.

27 Y. Alex, P. Ling, S. Filip, M. Miroslav, M. Stanislava, S. Zdenek and P. Martin, *ACS Nano*, 2013, **7**,

5930–5939
28 S. Rao, S. Jammalamadaka, A. Stesmans, V. Moshchalkov, J. Tol, D. Kosynkin, A. Higginbotham-Duque and J. Tour, *Nano Lett.*, 2012, **12**, 1210–1217.
29 J. Li, X. Li, P. Zhao, D. Y. Lei, W. Li, J. Bai, Z. Ren and X. Xu, *Carbon*, 2015, **84**, 460–468.
30 L. Quan, F. X. Qin, D. Estevez, H. Wang and H. X. Peng, *Carbon*, 2017, **125**, 630–639.
31 S. Wang, K. Hu, F. Huang, M. Zhang, S. Wu, Q. Liu and X. Kong, *Carbon*, 2019, **152**, 818–826.
32 Z. Sun, Z. Yan, K. Yue, A. Li and L. Qian, *Appl. Surf. Sci*, 2021, **538**, 147943.
33 Z. Sun, Z. Yan, K. Yue, A. Li and L. Qian, *Compos. B. Eng.*, 2020, **196**, 108132.
34 X. Chen, Y. Zhang, L. Tao, Q. Nie, F. Meng, S. Zhu, L. Cui and R. Huang, *Carbon*, 2020, **164**, 224–234.
35 W. Gu, J. Sheng, Q. Huang, G. Wang, J. Chen and G. Ji, *Nano-Micro Lett.*, 2021, **13**, 102.
36 Y. Lian, B. Han, D. Liu, Y. Wang, H. Zhao, P. Xu, X. Han and Y. Du, *Nano-Micro Lett.*, 2020, **12**, 153.
37 T. Hou, Z. Jia, Y. Dong, X. Liu and G. Wu, *Chem. Eng. J*, 2022, **431**, 133919.
38 H. Zhang, J. Cheng, H. Wang, Z. Huang, Q. Zheng, G. Zheng, D. Zhang, R. Che and M. Cao, *Adv. Funct. Mater.*, 2021, **32**, 2108194.
39 J. Cheng, H. Zhang, H. Wang, Z. Huang, H. Raza, C. Hou, G. Zheng, D. Zhang, Q. Zheng and R. Che, *Adv. Funct. Mater*, 2022, **32**, 2201129.
40 C. Xu, P. Liu, Z. Wu, H. Zhang, R. Zhang, C. Zhang, L. Wang, L. Wang, B. Yang, Z. Yang, W. You and R. Che, *Adv. Sci.*, 2022, **9**, e2200804.
41 M. Huang, X. Yu, L. Wang, J. Liu, W. You, M. Wang and R. Che, *Small Structures*, 2021, **2**, 2100033.
42 C. Wen, X. Li, R. Zhang, C. Xu, W. You, Z. Liu, B. Zhao and R. Che, *ACS Nano*, 2021, **16**, 1150–1159.
43 J. Xu, X. Zhang, Z. Zhao, H. Hu, B. Li, C. Zhu, X. Zhang and Y. Chen, *Small*, 2021, **17**, e2102032.
44 J. Liang, J. Chen, H. Shen, K. Hu, B. Zhao and J. Kong, *Chem. Mater.*, 2021, **33**, 1789–1798.
45 X. Zhang, Y. Shi, J. Xu, Q. Ouyang, X. Zhang, C. Zhu, X. Zhang and Y. Chen, *Nano-Micro Lett.*, 2021, **14**, 27.
46 J. Yang, J. Wang, H. Li, Z. Wu, Y. Xing, Y. Chen and L. Liu, *Adv. Sci.*, 2022, **9**, e2101988.
47 D. Lan, M. Qin, J. Liu, G. Wu, Y. Zhang and H. Wu, *Chem. Eng. J*, 2020, **382**, 122797.
48 D. Xu, Y. Yang, L. Lyu, A. Ouyang, W. Liu, Z. Wang, L. Wu, F. Yang, J. Liu and F. Wang, *Chem. Eng. J.*, 2021, **410**, 128295.
49 Z. Xu, Y. Du, D. Liu, Y. Wang, W. Ma, Y. Wang, P. Xu and X. Han, *ACS Appl. Mater. Interfaces*, 2019, **11**, 4268–4277.
50 R. Zhou, Y. Wang, Z. Liu, Y. Pang, J. Chen and J. Kong, *Nano-Micro Lett.*, 2022, **14**, 122.
51 Y. Hou, W. Yang, C. Zhong, S. Wu, Y. Wu, F. Liu, X. Huang and G. Wen, *Chem. Eng. J*, 2019, **378**, 122239.
52 M. Qin, L. Zhang, X. Zhao and H. Wu, *Adv. Sci.*, 2021, **8**, 2004640.
53 D. Lan, Z. Gao, Z. Zhao, G. Wu, K. Kou and H. Wu, *Chem. Eng. J*, 2021, **408**, 127313.
54 X. Xu, S. Shi, Y. Tang, G. Wang, M. Zhou, G. Zhao, X. Zhou, S. Lin and F. Meng, *Adv. Sci.*, 2021, **8**, 2002658.
55 C. Zhang, X. Li, Y. Shi, H. Wu, Y. Shen, C. Wang, W. Guo, K. Tian and H. Wang, *Adv. Opt. Mater.*, 2022, **10**, 2101904.
56 T. Li, D. Zhi, Y. Chen, B. Li, Z. Zhou and F. Meng, *Nano research*, 2020, **13**, 477–484.

57 R. Shu, G. Zhang, C. Zhang, Y. Wu, and J. Zhang, *Adv. Electron. Mater.*, 2021, **7**, 2001001.
58 H. Zhao, Y. Cheng, Z. Zhang, B. Zhang, C. Pei, F. Fan and G. Ji, *Carbon*, 2021, **173**, 501–511.
59 W. Yu and G. Shao, *J. Colloid Interface Sci.*, 2023, **640**, 680–687.
60 J. Zhou, J. Luo, G. Hao, F. Guo, G. Liu, H. Guo, G. Zhang, L. Xiao, Y. Hu and W. Jiang, *J. Mater. Chem. A*, 2022, **10**, 13848.
61 Q. Liu, L. Tang, J. Li, Y. Chen, Z. Xu, J. Li, X. Chen and F. Meng, *J. Mater. Sci. Technol.*, 2022, **130**, 166–175.
62 P. Wu, Y. F, J. Xu, Z. Fang, Q. Liu and X. Kong, *Carbon*, 2023, **202**, 194–203.
63 S. Hao, P. Liu and H. Wang, *J. Alloys Compd.*, 2023, **947**, 169454.
64 H. Ma, X. Zhang, L. Yang, L. Ma, C. Park, P. Gong and G. Li, *Carbon*, 2023, **205**, 159–170.
65 Q. Zhang, X. You, L. Tian, M. Wang, X. Zhang, Y. Shi, J. Yang and S. Dong, *J. Mater. Sci. Technol.* 2023, ***155***, 192–201.
66 K. Ran, W. Wang, X. Hou, Y. Huang, Z. Zhang, D. He, Y. Fang, S. Wang, R. Zhao and W. Xue, *J. Alloys Compd.*, 2022, **924**, 166568.
67 S. Shi, S. Ren, S. Hao, Y. Chen, C. Yang and S. Dai, *J. Mater. Sci*., 2022, **57**, 453–466.
68 M. Ling, F. Wu, P. Liu, Q. Zhang and B. Zhang, *small*, 2023, **19**, 2205925.